ADVANCED FUNCTIONAL MATERIALS
www.afm-journal.de
www.MaterialsViews.com

Mechanism of Phase Propagation During Lithiation in Carbon-Free $Li_4Ti_5O_{12}$ Battery Electrodes

*Chunjoong Kim, Nick S. Norberg, Caleb T. Alexander, Robert Kostecki, and Jordi Cabana**

Functional electrodes for batteries share a common design rule by which high electronic and ionic conductivity pathways must exist throughout the electrode in its pristine state. Notable amounts of conductive carbon additive in the composite electrode are usually included to form an electronically conductive matrix. However, excellent high rate cycling performance has been achieved in electrodes composed of the insulating $Li_4Ti_5O_{12}$ without any conductive additives. This behavior opens the possibility of a new paradigm for designing functional electrodes by which high electronic conductivity in the pristine electrode is not required. The mechanism of operation that enables such unexpected electrochemical behavior is evaluated and discussed. Electronically conductive pathways due to the reduction of Ti^{4+} to Ti^{3+} form and percolate throughout the $Li_4Ti_5O_{12}$ electrode in the early stage of Li insertion, eliminating the need for conductive additives. This work highlights the importance of the mass and charge transport properties of the intermediate states during cycling and of good interparticle ohmic contact in the electrode. This physical behavior can lead to novel system designs with improved battery utilization and energy density.

1. Introduction

Lithium-ion batteries continue to play a critical role in the development of modern portable digital and wireless technologies.[1,2] Their commercial success has triggered efforts to further expand its use to large-scale energy-storage applications, such as electric drive vehicles[3] and grid storage.[4,5] Growth of the lithium-ion battery market to these areas would enable deeper market penetration of sustainable energy sources, thus reducing consumption of fossil fuels. However, necessary performance improvements for these applications still require intensive research efforts aimed at improving existing or discovering better active or support materials.[6–12]

Electrochemical reactions in a battery involve the transport of ions between the electrodes and the electrolyte, and the transfer of electrons between the current collector and the electrode active material. In the case of Li-ion battery electrodes, this dual functionality is achieved with a porous composite electrode structure that consists of the active material, a conductive additive (typically, carbon black) and a binder, e.g., polyvinylidene difluoride (PVDF). However, the latter two are inactive toward reaction with Li^+, thereby lowering the specific energy (Wh/kg) and energy density (Wh/l) of the battery.

Titanium oxides are very attractive Li-ion battery negative electrode materials because they are inexpensive, non-toxic, and reversibly intercalate Li at a redox potential of around 1.5 V vs. Li^+/Li^0, above where electrolyte reduction reactions typically occur.[13,14] In particular, $Li_4Ti_5O_{12}$ has attracted considerable attention as an anode material due to its demonstrated high rate capabilities and excellent cyclability. Indeed, recent reports suggested $Li_4Ti_5O_{12}$-based Li-ion batteries are promising candidates for transportation applications because of their good stability and safety performance.[15,16] Li intercalation proceeds according to the following two-phase reaction:[17]

$$Li_4Ti_5O_{12} + 3Li^+ + 3e^- \leftrightarrow Li_7Ti_5O_{12} \quad (1)$$

The excellent cyclability is attributed to its nearly zero volume change between end members,[18] which minimizes mechanical strain that can degrade electrodes with repeated cycling.[19,20]

However, the vast majority of known, stable titanium oxides, including $Li_4Ti_5O_{12}$, are electronic insulators due to the presence of only Ti^{+4}, which has a d^0 electronic configuration. Satisfactory electrochemical performance of these materials has conventionally been achieved by using carbon-coated nanoparticles in order to both shorten Li^+ diffusion lengths[13,14] and provide a continuous electronically conductive network.[21] Interestingly, Song et al. recently reported that $Li_4Ti_5O_{12}$ can cycle effectively without any conductive additives.[22] The authors hypothesized that the origin of this surprising behavior was two-fold. Firstly, $Li_7Ti_5O_{12}$ is very electronically conductive, which enables high electron mobility in the lithiated state. Secondly, the slight crystal lattice

---

Dr. C. Kim, Dr. N. S. Norberg, C. T. Alexander,
Dr. R. Kostecki, Dr. J. Cabana
Environmental Energy Technologies Division
Lawrence Berkeley National Laboratory
Berkeley, CA 94720, USA
E-mail: jcabana@lbl.gov
C. T. Alexander
College of Chemistry
University of California Berkeley
Berkeley, CA 94720, USA

DOI: 10.1002/adfm.201201684

misfit between pristine and intercalated phases leads to the formation of stable interfaces at the lithiation front, which ensures good electron and ion transport across the interphase. The question persists, however, of how such lithiation occurs across a composite electrode that consists of an originally insulating material and is several tens of micrometers thick. In this work, the mechanism of phase transformation of $Li_4Ti_5O_{12}$ is studied by a combination of spectroscopic tools and the critical parameters responsible for this intriguing behavior are discussed.

2. Results and Discussion

2.1. Electrochemical Performance

$Li_4Ti_5O_{12}$ was synthesized by a solid-state reaction. The resulting powder was determined to be phase pure from its X-ray diffraction pattern (XRD, Figure S1a, Supporting Information), which was consistent with a spinel structure.[23] The sample exhibited the expected 4:5 atomic ratio of Li to Ti, as determined by inductively coupled plasma-atomic emission spectroscopy (ICP-AES). The $Li_4Ti_5O_{12}$ powder consisted of large agglomerates of primary ≈1 μm particles, as observed by scanning electron microscopy (SEM, Figure S1b, Supporting Information). The specific surface area was calculated to be ≈2.2 cm^2/g from BET adsorption isotherms.

40 and 80 μm thick carbon-free composite electrodes containing 90 wt% $Li_4Ti_5O_{12}$ powder and 10 wt% PVDF binder, with active material mass loadings of 4.4 and 10.7 mg/cm^2, respectively, were assembled in Li-metal half cells. These loadings are comparable to those in commercial, carbon-containing electrodes.[24] **Figure 1**a shows the discharge capacities at different rates of these electrodes compared to a 40 μm-thick electrode containing 10 wt% carbon black (CB) and 10 wt% PVDF binder ($Li_4Ti_5O_{12}$ loading: 4.28 mg/cm^2). An extended flat voltage plateau, indicative of a two-phase process,[17] was observed in all cases. The carbon-free electrodes exhibited strikingly high rate capabilities. Furthermore, the 40 μm thick carbon-free electrode attained slightly better capacities at the same rates than its equivalent with carbon additive. Even the ≈80 μm thick electrode showed excellent active material utilization, albeit at lower discharge rates. Extended cycling of the 40 μm-thick electrodes at a 1*C* rate (Figure 1b) resulted in 92% capacity retention after 100 cycles. In fact, no capacity loss was observed from the 5th cycle onwards; the fluctuation in specific capacity for cycles 10–80 was due to a fluctuation in laboratory temperature during the measurement. The charge-discharge coulombic efficiency is >97% for cycles 1–5, and 100% thereafter. These performance parameters for the carbon–free, micrometer-sized $Li_4Ti_5O_{12}$ electrodes were similar to electrodes with conductive carbon coated $Li_4Ti_5O_{12}$ nanopowders,[21] and were also consistent with the results reported by Song et al.[22]

Mechanical calendaring of the composite electrode at the end of the electrode assembly was a critical step to achieve this performance. While non-calendared, carbon-free electrodes exhibited only 20% of the theoretical capacity at *C*/10 (Figure S2, Supporting Information), close to 100% utilization was achieved after the calendaring. This observation suggests that the intimate electronic contact both between active material particles and with the Al foil current collector is essential. The importance of interparticle contact in enhancing the material utilization in carbon-free electrodes was recently highlighted by the successful cycling of carbon-free, sintered $LiCoO_2$ pellets up to 200 μm thick.[25] $LiCoO_2$ has higher electronic conductivity (e.g., ≈10^{-4} S/cm) than $Li_4Ti_5O_{12}$ (10^{-8} S/cm) in their pristine states,[26] and measurements were performed at lower rates than in this study. Nonetheless, sintering enabled high material utilization and a remarkable number of cycles due to the low interparticle contact resistance.

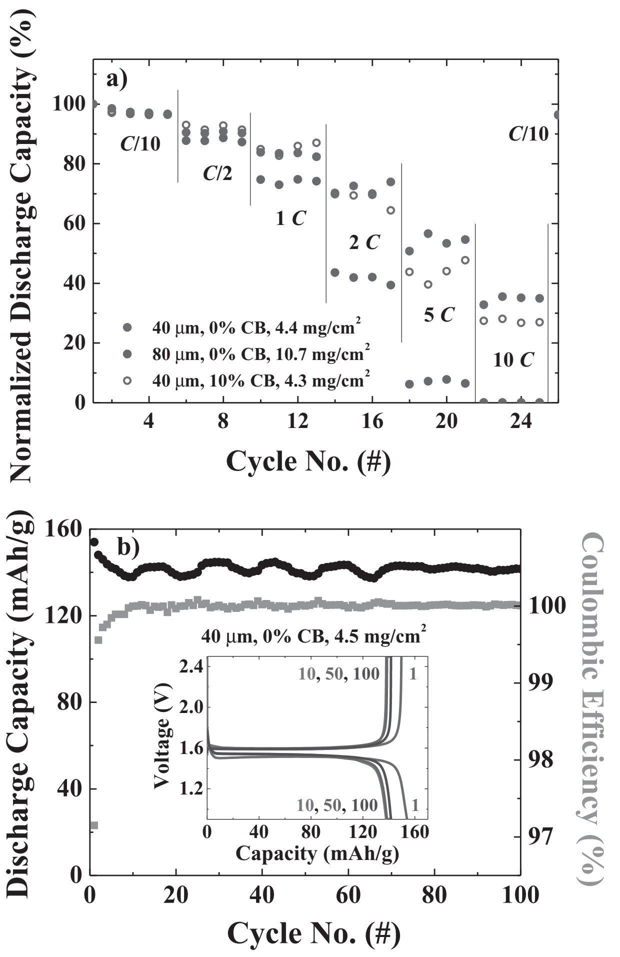

Figure 1. a) Discharge rate capabilities of different $Li_4Ti_5O_{12}$ electrodes in lithium metal half cells. The electrode thickness and carbon black additive (CB) weight% are indicated. All electrodes contained 10% PVDF. b) Specific capacity (black) and coulombic efficiency (gray) vs. cycle number of a 40 μm thick $Li_4Ti_5O_{12}$ electrode cycled in a lithium metal half cell at a 1*C* rate. The inset depicts the voltage-specific capacity profiles.

The two-phase redox transition at 1.55 V between $Li_4Ti_5O_{12}$ and $Li_7Ti_5O_{12}$ is very well known and characterized.[17,18,27] However, a few reports indicated that further Li insertion below ≈0.5 V is possible. Such insertion was proposed to occur simultaneously in the 8a and 16c sites of the spinel structure to form of $Li_9Ti_5O_{12}$, resulting in a theoretical capacity of 293 mAh/g.[28,29] This low-potential reaction also appeared to occur with a negligible volume change.[28] The carbon-free electrodes are valuable to study the mechanism of operation at low potentials without

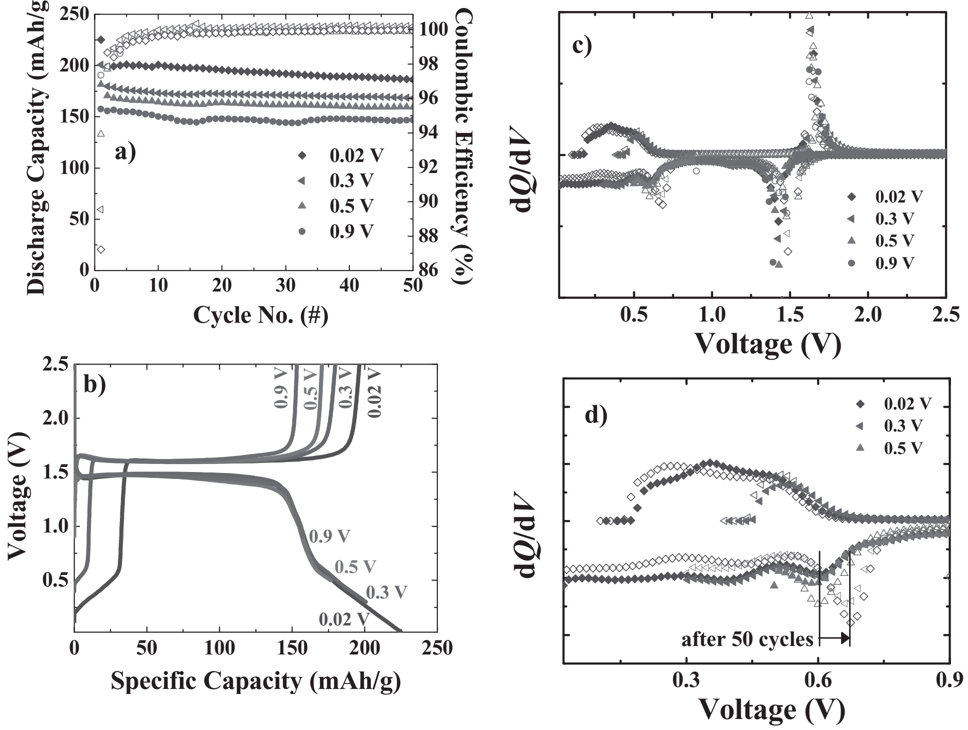

Figure 2. a) Specific discharge capacity (closed symbols) and coulombic efficiency (open symbols) vs. cycle number and b) voltage-specific capacity profiles of a 40 µm thick $Li_4Ti_5O_{12}$ electrode tested in lithium metal half cells at a 1*C* rate using different discharge cutoff potentials. c,d) d*Q*/d*V* vs. voltage plots of the 1st (closed symbols) and 50th cycles (open symbols) for the $Li_4Ti_5O_{12}$ electrodes, shown up to 2.5 V and 0.9 V, respectively.

possible interference from side effects due to the additives. **Figure 2**a displays the representative cyclability of 40 µm thick carbon-free $Li_4Ti_5O_{12}$ electrodes on Cu foil at a 1*C* rate, with discharge cut-off voltages of 0.9, 0.5, 0.3 and 0.02 V, respectively. The electrode discharge capacity in the first cycle progressively increased from 157 to 225 mAh/g as the cut-off potential was lowered. However, the corresponding charge-discharge coulombic efficiency decreased from 97% to 87%. Further insight into the lithiation process at low potentials was obtained from the analysis of the voltage profiles and the corresponding incremental charge (d*Q*/d*V*) plots (Figure 2b,c). Lithium insertion below 0.9 V occurred through a series of processes that resulted in a sloping potential profile. A cathodic peak at 0.6 V during the first discharge was not accompanied by a corresponding anodic peak. This process was most likely related to irreversible electrolyte decomposition. Interestingly, this peak shifted to 0.7 V after 50 cycles for the cells discharged to 0.3 and 0.02 V (Figure 2d), indicating continued reactivity and possible changes in the electrolyte decomposition mechanism. A notable degree of electrochemical reversibility was observed between 0.5 V and 0.02 V. At least part of this capacity could be assigned to the insertion of Li into $Li_7Ti_5O_{12}$.[28]

2.2. Characterization of Pristine and Cycled $Li_4Ti_5O_{12}$ Electrodes

The UV-Visible absorption spectrum of pristine $Li_4Ti_5O_{12}$ shows an absorption threshold at 330 nm with no features at lower energies (**Figure 3**a). Its estimated band gap energy of 3.8 eV, based on a plot of $(\alpha h\nu)^2$ vs. energy, was typical of electronically insulating materials and consistent with previously reported values.[30,31] A red-shift of the band gap energy and enhancement in electronic conductivity have been obtained in TiO_2 by the introduction of defects at the surface, such as oxygen vacancies which are charge-compensated by the presence of Ti^{3+}.[32] X-ray photoelectron spectra of the Ti 2p region of the pristine $Li_4Ti_5O_{12}$ powder showed that only Ti^{4+} was present on the surface (Figure 3b). In turn, the Raman spectrum of the powder (Figure 3c) was solely composed of five distinct active modes $3F_{2g}$ at 240, 263, and 365 cm^{-1}, E_g at 436 cm^{-1}, and A_{1g} at 674 cm^{-1} that are characteristic of the spinel structure.[33,34] No measurable signals were found at ≈1360 cm^{-1} and ≈1600 cm^{-1} which could be ascribed to the D- and G-band of carbonaceous materials. Furthermore, microcombustion analysis results indicated that no measurable carbon traces above 0.01% could be found. In other words, no extrinsic electronically conductive impurities were present in the samples.

Alternate current (AC) electrochemical impedance spectroscopy (EIS) revealed the existence of a slightly flattened high frequency semicircle followed by a low frequency tail (Figure 3d). The flattening may be indicative of multiple contributions from bulk and grain boundary resistances. The electrical conductivity was calculated to be 9.8×10^{-7} S/cm from the high frequency intercept of the impedance spectrum with the Z′ axis. The direct current (DC) relaxation measured in the same setup revealed that the electronic conductivity was at least two orders

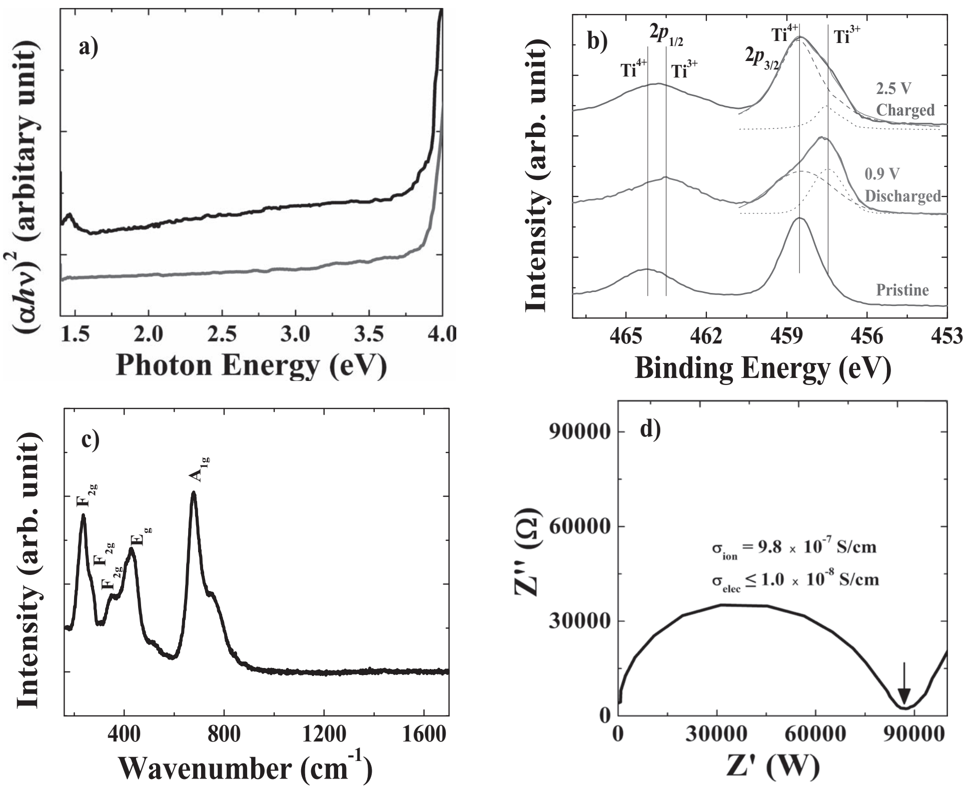

Figure 3. a) UV-vis absorption spectra of $Li_4Ti_5O_{12}$ particles scraped from a 40 µm thick carbon-free electrode before (gray) and after (black) discharging to 0.9 V. b) Ti 2p XPS of similar electrodes in the pristine state, after a discharge to 0.9 V, and after 1 cycle between 0.9 and 2.5 V. c) Raman spectrum of the pristine $Li_4Ti_5O_{12}$ electrode. d) Complex impedance plot at room temperature of $Li_4Ti_5O_{12}$ powder prepared in the form of a sintered pellet.

of magnitude smaller (≤1 × 10^{-8} S/cm, Figure S3, Supporting Information). This very low electronic conductivity would call for a conductive additive when following the standard electrode design rules used in Li-ion battery technology.[35] Pellet sintering ensured the low resistance at the interparticle contacts in this polycrystalline sample. Therefore, the low electronic conductivity of the compound and the shape of the Nyquist plot resulting from EIS (Figure 3d) indicate the measured AC impedance is attributed to purely ionic phenomena.[36] The measured electronic and ionic conductivities are in a good agreement with literature reports.[37,38]

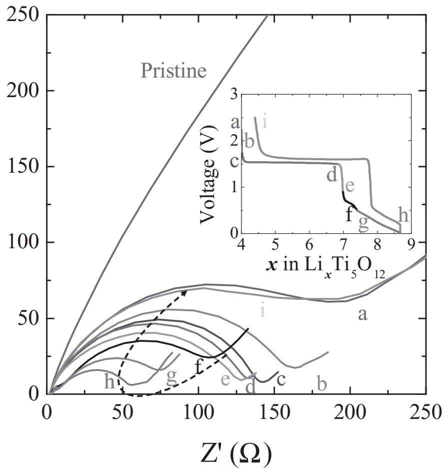

Figure 4. Electrochemical impedance spectra from a Li/1 M $LiPF_6$ in EC:DEC (45:55)/$Li_4Ti_5O_{12}$:PVDF (90:10) cell during the first cycle of Li (de)intercalation. The inset indicates the voltages at which data was collected.

In order to better understand the behavior of the carbon-free $Li_4Ti_5O_{12}$ electrodes upon cycling, EIS, together with ex situ XPS and UV-vis absorption spectroscopy data were collected during (de)lithiation. The very high impedance in the pristine state was related to the low electronic conductivity of $Li_4Ti_5O_{12}$ (**Figure 4**). However, it decreased significantly after intercalation of 0.01 mol Li^+ at 1.8 V (point a), suggesting that such low levels of intercalation are sufficient to dramatically increase the electronic conductivity of the electrode. A notably more moderate change in the impedance was observed between point a and c, just before the flat voltage plateau, which corresponds to a total of 0.05 mol Li^+. Little difference was also observed between both end points in the plateau (c,d). The electrode impedance continued to decrease upon discharging to 0.02 V. XPS confirmed the presence of Ti^{3+} at 0.9 V (Figure 3b), which was responsible for the drop in electrode resistivity. The electrochemical reduction of Ti^{4+} to Ti^{3+} was also reflected by the change of color of the electrodes from white to dark blue after discharge to 0.9 V (Figure S4, Supporting Information). This color was consistent with the formation of the intermediate trap states within the band gap. This effect manifested itself through the appearance of a UV-Vis optical absorption peak observed at 1.5 eV, as well as a gradual increase in absorption intensity below the band gap energy (Figure 3a). Nonetheless, the position of the bandgap remained unchanged. A similar sub-band gap absorption feature was also observed for n-doped and lithiated TiO_2.[39,40] In these complementary examples, absorption was determined to originate from excitation of electrons localized around Ti^{3+} to the conduction band.

The structural changes occurring during lithiation were monitored by in situ Raman spectroscopy. The technique is mainly sensitive to shallow depths and, thus, suitable for probing the top of the electrode, away from the current collector. A significant loss of the $Li_4Ti_5O_{12}$ Raman signal was observed after only ca. 0.3 mol Li was intercalated (**Figure 5**). In contrast to what was reported in the initial stages of Li intercalation into TiO_2,[41] no peak shift or splitting was observed before the loss of Raman signal. The lack of visible changes was taken as indication of the negligible solubility of Li in $Li_4Ti_5O_{12}$. The decrease in Raman intensity may be due to the limited penetration depth of the laser beam, δ, which is inversely proportional to the electronic conductivity of the material i.e., $\delta \propto (1/\sigma)^{1/2}$.[42,43] Thus, the rise in conductivity observed by EIS measurements (Figure 4a), related to the formation of $Li_7Ti_5O_{12}$, may have caused a reduction in the overall Raman intensity due to a limited light probe penetration depth. Lithium intercalation into $Li_4Ti_5O_{12}$ may have also induced significant deviations in the local symmetry of the crystalline lattice and affect its vibration modes. The Raman selection rules may no longer allow these modes, resulting in the signal intensity decrease upon incorporation of Li. At any rate, the loss of Raman signal cannot be explained by the formation of a thick film of electrolyte decomposition products, as the extent of such side reactions is considered to be minimal above 1.2 V. It was ascribed to the formation of $Li_7Ti_5O_{12}$ in the observed area.

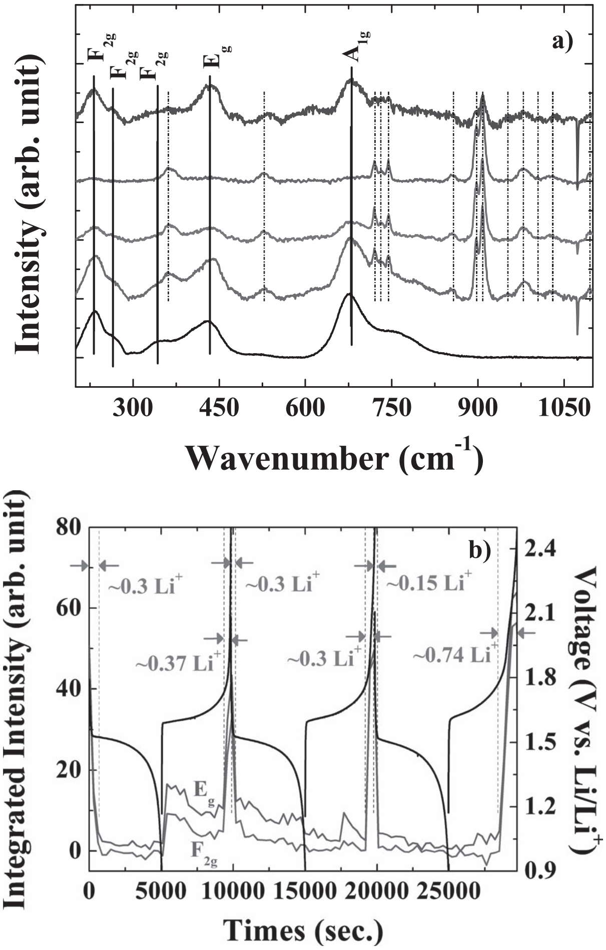

Figure 5. a) Selected spectra from in situ Raman spectroscopy measurements for a 40 μm carbon-free $Li_4Ti_5O_{12}$ electrode at different depths of discharge (DOD) during the first cycle. The Raman peaks due to electrolyte are indicated by dashed lines. b) Integrated Raman peak intensities of the E_g (436 cm^{-1}) and F_{2g} (365 cm^{-1}) bands of $Li_4Ti_5O_{12}$ measured in this in situ experiment, compared to the corresponding voltage-time profile.

The impedance of the cell increased after charging the electrode from 0.02 V to 2.5 V, but not to the levels of the pristine state (Figure 4a). Similar results were obtained when the cut-off voltage was set to 0.9 V (Figure S5, Supporting Information). Therefore, a small amount of Ti^{3+} remained even after delithiation, as confirmed by Ti 2p XPS (Figure 3b), consistent with the coulombic efficiencies of less than 100% in the first cycle. The electrode returned to its original white color, except for a slight light blue undertone (Figure S4, Supporting Information). This slight coloration provided additional evidence for the presence of Ti^{3+} sub-band gap states. Close inspection of the electrode revealed a macroscopic inhomogeneity indicative of gradients in distribution of this reduced species. Nonetheless, the fact that the impedance at this stage (point i in Figure 4a) did not exceed that of point a indicated that, despite not being homogeneous, the presence of electron carriers was sufficiently pervasive to produce percolation throughout the electrode. The intensity of the Raman signal in the in situ experiment recovered during deintercalation of the last ≈0.4 mol Li from the electrode (Figure 5), suggesting that the conductivity changes, and, hence, the phase transition, were highly reversible.

2.3. Model of Phase Transformation and Applicability to Other Systems

A scheme for the proposed mechanism of the phase propagation within the electrode is depicted in **Figure 6**. In the pristine state, the very low electronic conductivity of $Li_4Ti_5O_{12}$ implies that transfer of electrons can only happen at the points of contact between $Li_4Ti_5O_{12}$ particles and the current collector. The intimate contact between the active material and the metal foil induced by calendaring creates a heterogeneous interface. Bending of the conduction band in the space charge layer of the oxide occurs at this interface, which facilitates transport of electrons from metal to oxide. These phenomena would trigger the electrochemical reaction in close proximity to the foil. The Li^+ ions needed for this lithiation process come from the electrolyte in the pores of the composite electrode.

The huge increase in conductivity after intercalation of only 0.01 mol Li^+ suggests rapid electronic percolation throughout

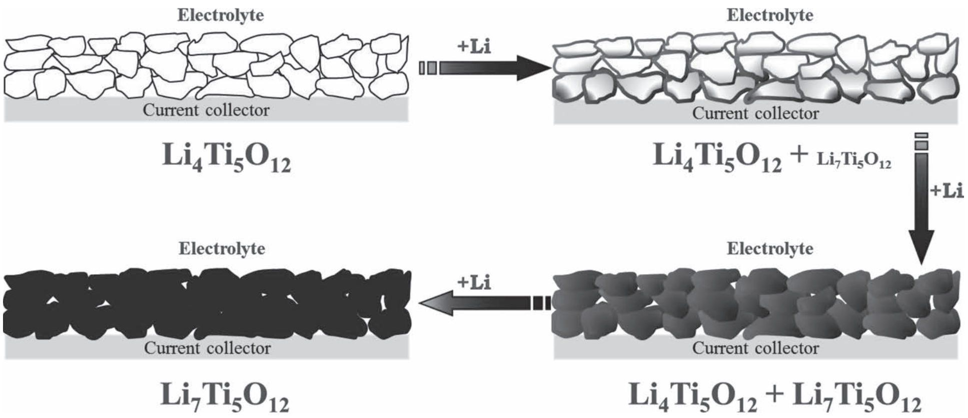

Figure 6. Scheme for the proposed lithiation mechanism in carbon-free $Li_4Ti_5O_{12}$ electrodes. In the very early stages of discharge, the highly conducting phase, $Li_{4+x}Ti_5O_{12}$, is formed in the vicinity of the current collector. The early propagation of this highly conducting phase across all active particle surfaces allows eventual lithiation of the whole electrode.

the electrode even at very low Li^+ intercalation levels. Inspection of the electrochemical curve at this stage revealed a sloping potential. Such behavior could be taken as indicative of some Li miscibility in $Li_4Ti_5O_{12}$ to form $Li_{4+\alpha}Ti_5O_{12}$ before segregation of the second phase, $Li_{7-\beta}Ti_5O_{12}$ ($\beta \neq 0$ if miscibility also exists on this end). However, the driving force for a reduction of the miscibility gap, namely, the interfacial penalty developed within a particle when the two end members are present,[44] does not exist in $Li_4Ti_5O_{12}/Li_7Ti_5O_{12}$[27] due to the almost zero lattice misfit.[17] Indeed, no evidence was found in the literature of the existence of solid solutions when the system is under electrical current,[17,18] which, in turn, is consistent with the lack of peak shift or splitting in the Raman spectra collected during Li intercalation. The much more pronounced increase in conductivity between pristine state and point a than between points a and c, still before the onset of the voltage plateau, would not be consistent with the formation of a solid solution, where the conductivity should scale linearly with the number of charge carriers.[45] Further, the conductivity changed even more slightly during the two-phase process (point c vs. d), where $Li_{7-\beta}Ti_5O_{12}$, a much more electron conductive phase based on the number of charge carriers, forms. Such slight change can only be explained by the fact that this high electron conductivity phase already formed a percolated network at point c. If the formation of $Li_{7-\beta}Ti_5O_{12}$ already takes place after only 0.01 mol Li are intercalated, the miscibility of Li in $Li_{4+\alpha}Ti_5O_{12}$ must be negligible, i.e., $\alpha \rightarrow 0$. Given the symmetry of the electrochemical curve, it is highly likely that $\beta \rightarrow 0$ as well. The appearance of this second phase at notably higher potentials than the plateau could be a reflection that intercalation into surface sites occurs at different potential with respect to the bulk.[27,46] A mechanism by which rapid percolation of the lithiated, highly conductive phase, $Li_7Ti_5O_{12}$, occurs also explains the appearance of this phase at the top surface of the electrode, as probed by in situ Raman spectroscopy. The low contact resistance between the oxide particles after calendaring ensures that the electrochemical reaction propagates throughout the whole electrode. However, at such low levels of lithiation, phase propagation must happen primarily across particle surfaces from the current collector to the electrode surface, which is 40 μm away. Once the conduction path is provided, the electrochemical reaction proceeds through the bulk of the $Li_4Ti_5O_{12}$ particles. In the case of the thick 80 μm electrode, depletion of Li^+ in the pores in the vicinity of the current collector limits cycling rates due to the increased tortuosity for Li^+ migration in thicker electrodes.[47]

To verify if similar functionality could apply to other materials, galvanostatic cycling was performed at a $C/10$ on carbon-free rutile TiO_2 (r-TiO_2), $LiNi_{1/2}Mn_{3/2}O_4$, and $LiCoO_2$ with similar microstructures (**Figure 7**). Similar to $Li_4Ti_5O_{12}$, lithiation of r-TiO_2 to form $Li_{\sim 0.5}TiO_2$, the most widely observed final state, creates a mixture of Ti^{4+}/Ti^{3+} in the lattice.[48] Due to the low electronic conductivity of the pristine r-TiO_2, with Ti present only with an oxidation state of 4+, nanoscale dimensions were considered to be required for acceptable electrode performance.[13,14] However, the carbon-free rutile electrode, composed of micron-size primary structures, could be lithiated to more than 95% of its theoretical capacity (Figure 7a), again challenging the existing rules of design. Nevertheless, the capacity fading, even at these low rates, is much worse compared to $Li_4Ti_5O_{12}$. Meanwhile, up to ≈25% and ≈30% of the theoretical capacity of the $LiNi_{1/2}Mn_{3/2}O_4$ (147 mAh/g) and $LiCoO_2$ (140 mAh/g for Li_xCoO_2, where $0 \leq x \leq 0.5$) electrodes[10] were achieved at $C/10$. In the case of the Ni-containing spinel oxide, performance was compromised by the absence of highly electronically conductive intermediate phases during the electrochemical reaction.[49] This behavior was taken as further indication that formation of electronically conductive intermediates is necessary for electronic percolation from the current collector to the whole electrode. The fact that carbon-free, sintered pellets of $LiCoO_2$, which undergoes a transition to a metallic state upon lithium extraction, were found to be functional as electrodes provides support for this rule.[26] The poor cycling performance of the $LiCoO_2$ and r-TiO_2 electrodes highlighted that a second fundamental requirement for carbon-free electrodes is the preservation of interparticle contact.[50] While $Li_4Ti_5O_{12}$ effectively undergoes no volume change during cycling, $LiCoO_2$

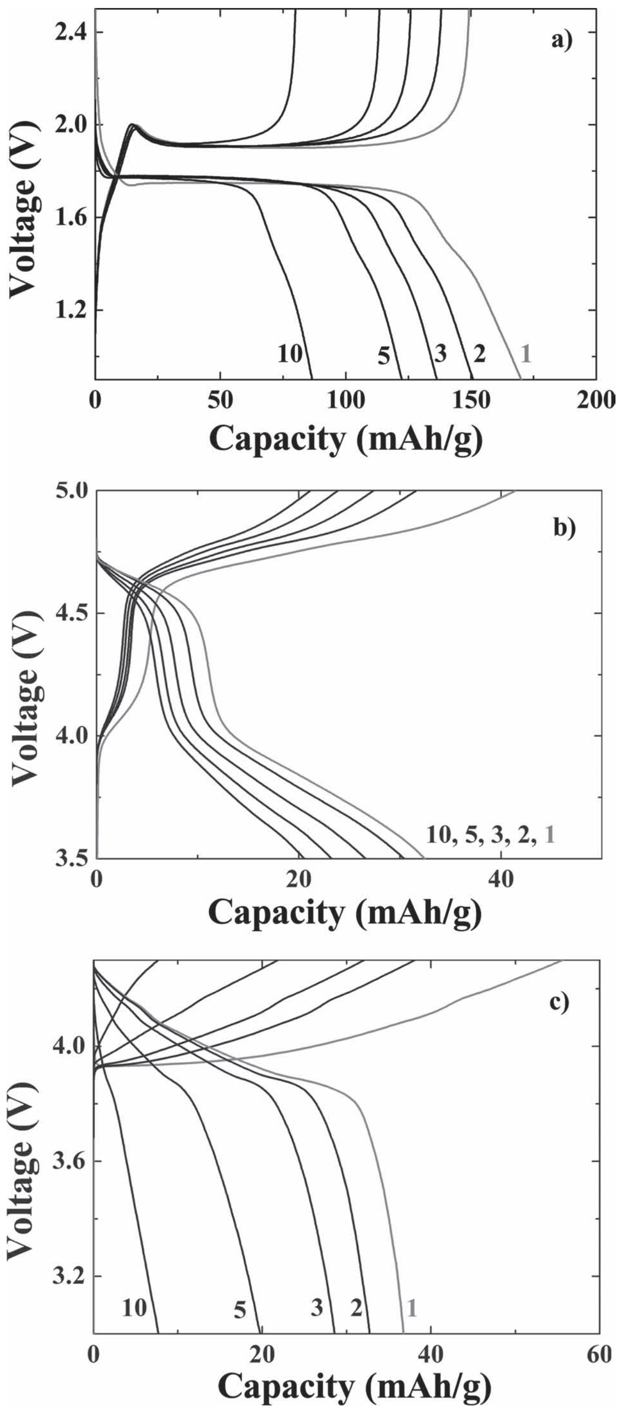

Figure 7. Galvanostatic charge/discharge curves for selected cycles of carbon-free a) r-TiO_2, b) $LiNi_{0.5}Mn_{1.5}O_4$, and c) $LiCoO_2$ electrodes in lithium half cells at *C*/10 rate. The gray lines indicate the first cycle of each experiment.

and r-TiO_2 exhibit anisotropic volume changes of ≈2% and 6%, respectively.[48,51] Such misfit builds up strain within the particles and at the oxide-oxide interfaces which eventually leads to the loss of contact.[52] The result is the poor electrochemical activity, even though the intermediate phases are conductive. Good contact between particles can be preserved by sintering the active material in a pellet, but this structure will also increase the pore tortuosity, hence, reducing the rate capabilities of the electrode as the Li^+ concentration will be depleted at electrode surfaces upon high lithiation rates.[25]

3. Conclusions

The current paradigm in which Li-ion battery composite electrodes must have high electronic conductivity in their pristine state is not universal. Electrochemical cycling of carbon-free electrodes made with insulating $Li_4Ti_5O_{12}$ was possible at rates as high as 10*C*. The underlying reason for this exceptional performance is the early formation of mixed Ti^{4+}/Ti^3 surface oxidation states that are highly electronically conductive. The initial conducting phase transformation occurs in the vicinity of the current collector, but rapidly propagates toward the surface of the electrode at very early stages of lithiation. This work also highlights the importance of optimizing interparticle contact in order to minimize the need for conductive additives in composite electrodes. This aspect becomes particularly important when using nanostructured materials, as current synthetic methodologies lead to poorly packed particles compared to micrometer-sized materials. Work is currently underway to further establish the generality of this model and verify the mechanistic hypothesis. From the practical point of view, this report contributes to bringing the battery field closer to the maximization of energy density in Li-ion devices through the minimization of inactive components in the electrode. Further gains could be achieved by designing electrodes that closely tailor particle assembly while optimizing the pore structure to reduce tortuosity. Creating such structures at thicknesses that enable high active material areal loadings constitutes a fascinating challenge for the materials science community.

4. Experimental Section

Materials Preparation: $Li_4Ti_5O_{12}$ was synthesized by a solid state reaction using TiO_2 (Sigma Aldrich, anatase, ≥99%) and Li_2CO_3 (Sigma Aldrich, 99%). 5 mole% excess TiO_2 and Li_2CO_3 were well mixed and then heated at 850 °C for 5 h with a heating and cooling rate of 5 °C/min.

Physical Characterization: Powder X-ray diffraction was performed on a Phillips X'Pert diffractometer with an X'celerator detector using Cu Kα radiation. Scanning electron microscopy (SEM) images were obtained using a JEOL JSM-7500F field-emission microscope in gentle beam mode at 1 kV. Elemental analyses and micro-combustion were carried out at Columbia Analytical Services (Tucson, AZ). UV-vis absorption spectra were recorded on solutions of $Li_4Ti_5O_{12}$ that was scraped from an electrode and dispersed in ethanol by means of a UV-vis spectrophotometer (DU-65, Beckman). The specific surface area of the $Li_4Ti_5O_{12}$ particles was calculated from Brunauer–Emmett–Teller (BET) analysis of nitrogen adsorption measurements (TriStar II 3020). X-ray photoelectron spectroscopy (XPS) was conducted using a Sigma Probe from Thermo that is stationed in a glove box in order to minimize air exposure.

Electrical conductivity measurements were performed on a pellet of as-synthesized powder $Li_4Ti_5O_{12}$ with a diameter of ca. 28 mm and a thickness of ca. 1.4 mm that was pressed to 1.0 ton/cm^2 and heated at 850 °C for 8 h. Gold thin films were then sputtered on both sides of the pellet to serve as electrodes. AC impedance measurements were performed in a frequency range from 1 MHz to 200 mHz. The DC polarization measurement was calculated from the decayed direct current after a 100 000 s relaxation time upon applying a 0.7 V potential on the pellet.

Electrochemical Measurements: The working electrodes were prepared by mixing a slurry of $Li_4Ti_5O_{12}$, carbon black (CB), and polyvinylidene difluoride (PVDF) in *N*-methyl pyrrolidone (NMP) with a mass ratio of 80:10:10 or 90:0:10, casting the slurry on pure aluminum or copper foil, and drying the electrode under vacuum at 110 °C overnight. Dried electrodes were calendared with a line pressure of 600 kgf/cm with a roll press (IRM Lab Mill Table Model). 2032 type coin cells were assembled in an Ar-filled glove box (water and oxygen ≤ 0.1 ppm) with $Li_4Ti_5O_{12}$ as the working electrode, high-purity lithium foil (Sigma Aldrich) as the counter electrode, Celgard 2500 as the separator, and electrolyte composed of 1 M $LiPF_6$ in a mixture of ethylene carbonate (EC) and diethyl carbonate (DEC) with a volume ratio of 45:55 (Novolyte Technologies). Charge-discharge measurements of $Li_4Ti_5O_{12}$ vs. Li^+/Li^0 were recorded on a Biologic VMP3 potentiostat at room temperature under different rates with discharge cut-off voltages ranging from 0.02 V to 0.9 V. The charge cut-off voltage was fixed at 2.5 V in all cases. The rate was defined as C/n, where $C = 175$ mA/g corresponded to the theoretical charge capacity of the electrode, and n was defined as the discharge time (in hours). In situ impedance spectroscopy measurements were performed on $Li_4Ti_5O_{12}$ coin cells at the end point of every step shown in the inset of Figure 4a during a discharge and charge at a $C/10$ rate.

In situ Raman spectroscopy measurements were recorded using a custom-built three-electrode, spectro-electrochemical cell. A polypropylene cell body was equipped with a working electrode (stainless steel rod embedded in a polypropylene sheath) and counter and reference electrodes (two stainless steel connectors covered with Li-foil) located in a reservoir filled with electrolyte composed of 1 M $LiPF_6$ in ethylene carbonate (EC) and diethyl carbonate (DEC) with a weight ratio of 2:1 (Novolyte Technologies). A glass optical window above the working electrode provided a clear path for Raman measurements. A 7 mm diameter, 40 mm thick $Li_4Ti_5O_{12}$ electrode was attached to the stainless steel rod of the spectro-electrochemical cell with conductive epoxy (CW2400, Circuitworks) and insulated with a standard epoxy (Torr Seal, Varian, Inc.). The electrode was cycled galvanostatically for three cycles at a $C/10$ rate between 2.5 and 0.9 V using a Gamry Reference 600 potentiostat/galvanostat. In situ Raman spectra were collected with a "Labram" Raman microscope system from ISA Groupe Horiba. The samples were excited with a 488 nm Ar^+ ion laser with the power adjusted to ≤ 2 mW. The system was setup in the backscattering configuration with an 80× objective, providing a beam diameter of ≈ 2 μm. A Raman spectrum was collected from the same spot every five minutes during electrochemical cycling.

Supporting Information

Supporting Information is available from the Wiley Online Library or from the author.

Acknowledgements

This work was supported by the Assistant Secretary for Energy Efficiency and Renewable Energy, Office of Vehicle Technologies of the U.S. Department of Energy under Contract No. DE-AC02-05CH11231, under the Batteries for Advanced Transportation Technologies (BATT) Program. CTA was supported by LBNL through the Science Undergraduate Laboratory Internship program from the Department of Energy.

Received: June 21, 2012
Revised: September 1, 2012
Published online: October 4, 2012

[1] M. Armand, J.-M. Tarascon, *Nature* **2008**, *451*, 652.
[2] J. B. Goodenough, Y. Kim, *Chem. Mater.* **2010**, *22*, 587.
[3] F. T. Wagner, B. Lakshmanan, M. F. Mathias, *J. Phys. Chem. Lett.* **2010**, *1*, 2204.
[4] B. Dunn, H. Kamath, J.-M. Tarascon, *Science* **2011**, *334*, 928.
[5] Z. Yang, J. Zhang, M. C. W. Kintner-Meyer, X. Lu, D. Choi, J. P. Lemmon, J. Liu, *Chem. Rev.* **2011**, *111*, 3577.
[6] M. M. Thackeray, S.-H. Kang, C. S. Johnson, J. T. Vaughey, R. Benedek, S. A. Hackney, *J. Mater. Chem.* **2007**, *17*, 3112.
[7] J. Cho, Y.-W. Kim, B. Kim, J.-G. Lee, B. Park, *Angew. Chem. Int. Ed.* **2003**, *42*, 1618.
[8] J. Cabana, L. Monconduit, D. Larcher, M. R. Palacín, *Adv. Mater.* **2010**, *22*, E170.
[9] C.-M. Park, J.-H. Kim, H. Kim, H.-J. Sohn, *Chem. Soc. Rev.* **2010**, *39*, 3115.
[10] B. L. Ellis, K. T. Lee, L. F. Nazar, *Chem. Mater.* **2010**, *22*, 691.
[11] G. Liu, S. Xun, N. Vukmirovic, X. Song, P. Olalde-Velasco, H. Zheng, V. S. Battaglia, L. Wang, W. Yang, *Adv. Mater.* **2011**, *23*, 4679.
[12] W.-R. Liu, M.-H. Yang, H.-C. Wu, S. M. Chiao, N.-L. Wu, *Electrochem. Solid-State Lett.* **2005**, *8*, A100.
[13] D. Deng, M. G. Kim, J. Y. Lee, J. Cho, *Energy Environ. Sci.* **2009**, *2*, 818.
[14] Z. Yang, D. Choi, S. Kerisit, K. M. Rosso, D. Wang, J. Zhang, G. Graff, J. Liu, *J. Power Sources.* **2009**, *192*, 588.
[15] K. Amine, I. Belharouak, Z. Chen, T. Tran, H. Yumoto, N. Ota, S.-T. Myung, Y.-K. Sun, *Adv. Mater.* **2010**, *22*, 3052.
[16] H.-G. Jung, M. W. Jang, J. Hassoun, Y.-K. Sun, B. Scrosati, *Nat. Commun.* **2011**, *2*, 516.
[17] S. Scharner, W. Weppner, P. Schmid-Beurmann, *J. Electrochem. Soc.* **1999**, *146*, 857.
[18] M. Wagemaker, D. R. Simon, E. M. Kelder, J. Schoonman, C. Ringpfeil, U. Haake, D. Lützenkirchen-Hecht, R. Frahm, F. M. Mulder, *Adv. Mater.* **2006**, *18*, 3169.
[19] J. Haetge, P. Hartmann, K. Brezesinski, J. Janek, T. Brezesinski, *Chem. Mater.* **2011**, *23*, 4384.
[20] H.-G. Jung, S.-T. Myung, C. S. Yoon, S.-B. Son, K. H. Oh, K. Amine, B. Scrosati, Y.-K. Sun, *Energy Environ. Sci.* **2011**, *4*, 1345.
[21] E. Kang, Y. S. Jung, G.-H. Kim, J. Chun, U. Wiesner, A. C. Dillon, J. K. Kim, J. Lee, *Adv. Funct. Mater.* **2011**, *16*, 492.
[22] M.-S. Song, A. Benayad, Y.-M. Choi, K.-S. Park, *Chem. Commun.* **2012**, *48*, 516.
[23] I. A. Leonidov, O. N. Leonidova, L. A. Perelyaeva, R. F. Samigullina, S. A. Kovyazina, M. V. Patrakeev, *Phys. Solid State* **2003**, *45*, 2183.
[24] K. A. Striebel, A. Sierra, J. Shim, C.-W. Wang, A. M. Sastry, *J. Power Sources* **2004**, *134*, 241.
[25] W. Lai, C. K. Erdonmez, T. F. Marinis, C. K. Bjune, N. J. Dudney, F. Xu, R. Wartena, Y.-M. Chiang, *Adv. Mater.* **2010**, *22*, E139.
[26] J. Molenda, A. Stokłosa, T. Bąk, *Solid State Ionics* **1989**, *36*, 53.
[27] W. J. H. Borghols, M. Wagemaker, U. Lafont, E. M. Kelder, F. M. Mulder, *J. Am. Chem. Soc.* **2009**, *131*, 17786.
[28] H. Ge, N. Li, D. Y. Li, C. S. Dai, D. L. Wang, *J. Phys. Chem. C* **2009**, *113*, 6324.
[29] Z. Zhong, C. Ouyang, S. Shi, M. Lei, *Chem. Phys. Chem.* **2008**, *9*, 2104.
[30] D. G. Kellerman, N. A. Mukhina, N. A. Zhuravlev, M. S. Valova, V. S. Gorshkov, *Phys. Solid State* **2010**, *52*, 459.
[31] T. Kostlánová, J. Dědeček, P. Krtil, *Electrochim. Acta* **2007**, *52*, 1847.
[32] U. Diebold, *Surf. Sci. Rep.* **2003**, *48*, 53.
[33] J. Shu, M. Shui, D. Xu, S. Gao, T. Yi, D. Wang, X. Li, Y. Ren, *Ionics* **2011**, *17*, 503.
[34] M. Kalbac, M. Zukalova, L. Kavan, *J. Solid State Eletrochem.* **2003**, *8*, 2.
[35] G. Liu, H. Zheng, A. S. Simens, A. M. Minor, X. Song, V. S. Battaglia, *J. Electrochem. Soc.* **2007**, *154*, A1129.
[36] J. Jamnik, J. Maier, *J. Electrochem. Soc.* **1999**, *146*, 4183.

[37] J. Wolfenstine, J. L. Allen, *J. Power Sources* **2008**, *180*, 582.
[38] C. H. Chen, J. T. Vaughey, A. N. Jansen, D. W. Dees, A. J. Kahaian, T. Goacher, M. M. Thackeray, *J. Electrochem. Soc.* **2001**, *148*, A102.
[39] J. H. Richter, A. Henningsson, P. G. Karlsson, M. P. Andersson, P. Uvdal, H. Siegbahn, A. Sandell, *Phys. Rev. B* **2005**, *71*, 235418.
[40] B. J. Morgan, G. W. Watson, *Phys. Rev. B* **2010**, *82*, 144119.
[41] L. J. Hardwick, M. Holzapfel, P. Novák, L. Dupont, E. Baudri, *Electrochim. Acta* **2007**, *52*, 5357.
[42] M. Inaba, Y. Todzuka, H. Yoshida, Y. Grincourt, A. Tasaka, Y. Tomida, Z. Ogumi, *Chem. Lett.* **1995**, *24*, 889.
[43] R. Baddour-Hadjean, J.-P. Pereira-Ramos, *Chem. Rev.* **2010**, *110*, 1278.
[44] M. Wagemaker, F. M. Mulder, A. Van der Ven, *Adv. Mater.* **2009**, *21*, 2703.
[45] J.-Y. Shin, J. H. Joo, D. Samuelis, J. Maier, *Chem. Mater.* **2011**, *24*, 543.
[46] L. Wang, F. Zhou, Y. S. Meng, G. Ceder, *Phys. Rev. B* **2007**, *76*, 165435.
[47] I. V. Thorat, D. E. Stephenson, N. A. Zacharias, K. Zaghib, J. N. Harb, D. R. Wheeler, *J. Power Sources* **2009**, *188*, 592.
[48] W. J. H. Borghols, M. Wagemaker, U. Lafont, E. M. Kelder, F. M. Mulder, *Chem. Mater.* **2008**, *20*, 2949.
[49] M. Mohamedi, M. Makino, K. Dokko, T. Itoh, I. Uchida, *Electrochim. Acta* **2002**, *48*, 79.
[50] M. Kerlau, M. Marcinek, V. Srinivasan, R. M. Kostecki, *Electrochim. Acta* **2007**, *52*, 5422.
[51] M. Morcrette, Y. Chabre, G. Vaughan, G. Amatucci, J.-B. Leriche, S. Patoux, C. Masquelier, J-M. Tarascon, *Electrochim. Acta* **2002**, *47*, 3137.
[52] N. Meethong, H.-Y. S. Huang, S. A. Speakman, W. C. Carter, Y.-M. Chiang, *Adv. Funct. Mater.* **2007**, *17*, 1115.